JOURNAL OF SPACECRAFT AND ROCKETS
Vol. 45, No. 3, May–June 2008

# Separation Motion of Strap-On Boosters with Base Flow and Turbulence Effects

Soon-Heum Ko* and Chongam Kim†
*Seoul National University, Seoul 151-742, Republic of Korea*

DOI: 10.2514/1.33706

**A numerical investigation is conducted around a multistage launch vehicle to examine the influence of the base region and turbulence. A Reynolds-averaged Navier–Stokes flow solver coupled with rigid body dynamics, because of resultant aerodynamic forces and gravity, is developed to simulate the detachment motion of strap-on boosters. An overset mesh technique is adopted to achieve maximal efficiency in simulating the relative motion of launch vehicles, and various turbulence models are implemented to accurately predict aerodynamic forces in high Reynolds number flows. The flow solver is validated by comparing the computed pressure coefficients of the Titan-IV launch vehicle with the experimental data. In addition, some preliminary studies are conducted to examine the influence of the base flow and turbulence effect in the accurate simulation of detachment motion. Finally, the separation behavior of the KSR-III, a three-stage sounding rocket developed in Korea, is numerically investigated. It is observed that the afterbody flowfield strongly affects the separation motion of strap-on boosters. The negative pitching moment of a strap-on at the initial stage of a detachment motion is gradually recovered and the final result is a safe separation, whereas forebody-only analysis yields a collision scenario between the core rocket and the booster. Only a slight difference in vehicle trajectory is observed from the comparison between inviscid and turbulent analyses. Change of the separation trajectory due to viscous effects is just a few percentage points and, therefore, inviscid analysis seems to be sufficient for the simulation of separation motion if the study focuses on the movement of strap-ons.**

## Nomenclature

| | | |
|---|---|---|
| $C_p$ | = | pressure coefficient |
| $C_\mu$ | = | eddy viscosity coefficient |
| $d\bar{s}$ | = | displacement vector, m |
| $d\alpha$ | = | angular displacement vector, deg |
| $\hat{E}, \hat{F}, \hat{G}$ | = | flux vectors |
| $\hat{E}_v, \hat{F}_v, \hat{G}_v$ | = | viscous flux vectors |
| $\bar{F}$ | = | resultant force vector, $\mathrm{kg} \cdot \mathrm{m/s^2}$ |
| $F_x, F_y, F_z$ | = | scalar components of $\bar{F}$ |
| $\bar{h}$ | = | angular momentum vector, $\mathrm{kg} \cdot \mathrm{m/s^2}$ |
| $I$ | = | identity matrix |
| $I_{ij}$ | = | moment of inertia, $\mathrm{kg} \cdot \mathrm{m^2}$ |
| $J$ | = | flux Jacobian |
| $\bar{M}$ | = | resultant moment vector about mass center, $\mathrm{kg} \cdot \mathrm{m^2/s^2}$ |
| $M_x, M_y, M_z$ | = | scalar components of $\bar{M}$ |
| $m$ | = | mass, kg |
| $p$ | = | pressure, $\mathrm{kg/(m \cdot s^2)}$ |
| $\hat{Q}$ | = | conservative variable vector |
| $\hat{R}$ | = | residual vector |
| $t$ | = | physical time, s |
| $\rho$ | = | density, $\mathrm{kg/m^3}$ |
| $\tau$ | = | pseudotime |
| $\bar{v}$ | = | velocity vector, m/s |
| $\bar{\omega}$ | = | angular velocity vector, 1/s |

Presented as Paper 277 at the 44th AIAA Aerospace Sciences Meeting and Exhibit, Reno, Nevada, 9–12 January 2006; received 26 July 2007; revision received 22 October 2007; accepted for publication 22 October 2007. 

*Doctoral Candidate, School of Mechanical and Aerospace Engineering, 599 Gwanangno, Gwanak-Gu; floydfan@snu.ac.kr.

†Associate Professor, School of Mechanical and Aerospace Engineering and the Institute of Advanced Aerospace Technology; 599 Gwanangno, Gwanak-Gu; chongam@snu.ac.kr. Senior Member AIAA.

## I. Introduction

STRAP-ON boosters have traditionally been used to increase the payload of launch vehicles. From an aerodynamic point of view, the boosters should guarantee minimal drag while maximizing payload capacity. However, even an optimal aerodynamic booster shape for steady flight may sometimes result in an unsafe trajectory after detachment from the core rocket. This may lead to a collision with the core rocket. Thus, it is important to investigate in detail the separation behavior of strap-on boosters and reflect on their aerodynamic dynamic characteristics during the design process. If a collision occurs during free fall, it then becomes mandatory to conduct extensive simulations using various jettisoning forces to find the optimal jettisoning conditions for a safe separation.

Many researchers have analyzed the aerodynamic dynamic behavior of launch vehicle configurations with strap-on boosters. Some researchers have conducted steady-state numerical and experimental flow analyses around the core rocket with a number of strap-on boosters [1–3]. Others have analyzed unsteady flowfield characteristics during separation based on the prescribed trajectory of strap-ons from experimental data [4–6]. As for the coupled analysis of aerodynamics and dynamics, unsteady simulation techniques with 6-degrees-of-freedom rigid body motions have been implemented into well-known flow codes such as OVERFLOW [7] or CFL3D. Various numerical analyses including store separation simulations using an overset or Cartesian grid technique [8,9], detachment of strap-ons from the core rocket [10], and impact of multiple bodies in proximate flight [11] have also been carried out. Recently, much research has focused on implementing appropriate turbulence models to describe the turbulent flowfields around projectiles [12–14] or constructing efficient aerodynamic databases to directly predict the trajectory of detached boosters from existing data sets [15].

Though remarkable progress has been made in this area, further research is still necessary. Firstly, most studies assumed the predefined trajectories of strap-on boosters from experimental data and simulated unsteady flowfields at given positions. Thus, numerical analyses were dependent on experimental data, even though the level of numerical modeling was sufficiently acceptable. Also, most aerodynamic dynamic coupled analyses focused on the forebody flow region only. Obviously, forebody flow analysis does not accurately predict the downward motion of boosters, because the

lower part of boosters will move out of the main computational domain during separation [1–6,10]. Secondly, regarding the implementation of turbulence models, steady-state flow analyses have mainly been conducted. The effect of turbulence on the separation dynamics of strap-ons needs to be more thoroughly investigated [12–14]. Finally, a data-driven simulation approach can be a powerful tool for the efficient prediction of separation motion, because it will substantially reduce the total computation time. However, this can only be realized if macrodata sets with various inflow conditions are provided. In addition, this approach does not provide local flow features during separation [15].

Keeping these things in mind, the current study focuses on improving the first and second shortcomings of these previous analyses. To examine the afterbody flow effect on separation motion, aerodynamic dynamic coupled simulations are conducted with forebody and full-body mesh systems. Numerical error in the forebody flow analysis is then investigated quantitatively by comparing the result with the full-body flow analysis. Regarding the effect of turbulence, the Reynolds-averaged Navier–Stokes (RANS) flow solver with the $k$–$\omega$ shear stress transport (SST) [16] two-equation model and the Spalart–Allmaras (SA) [17] one-equation model, which has been validated in various steady/unsteady applications [18–20], is adopted for efficient computations of high Reynolds-number viscous flows. For the current research, the Craft–Launder–Suga (CLS) [21] two-equation model is additionally introduced to the existing flow solver, and the three turbulence models are used for flow analyses of a prototype launch vehicle. From the computed results, a turbulence model with good accuracy and acceptable efficiency is chosen for the separation analysis of a multistage launch vehicle. Finally, the booster trajectory is compared with the inviscid counterpart to quantify the viscous effect.

## II. Numerical Approaches

### A. Flow Analysis

Because the present geometry contains massive flow separation in the base region, the three-dimensional compressible Navier–Stokes equations are adopted. The Navier–Stokes equations can be written in general curvilinear coordinates of $(\xi, \eta, \zeta)$ as follows:

$$\frac{\partial \hat{Q}}{\partial t} + \frac{\partial \hat{E}}{\partial \xi} + \frac{\partial \hat{F}}{\partial \eta} + \frac{\partial \hat{G}}{\partial \zeta} = \frac{1}{Re}\left(\frac{\partial \hat{E}_v}{\partial \xi} + \frac{\partial \hat{F}_v}{\partial \eta} + \frac{\partial \hat{G}_v}{\partial \zeta}\right) \tag{1}$$

where $\hat{Q}$ is the conservative variable vector, $\hat{E}$, $\hat{F}$, $\hat{G}$ are the inviscid flux vectors, and $\hat{E}_v$, $\hat{F}_v$, $\hat{G}_v$ are the viscous flux vectors.

For an adequate description of turbulent flowfield within the framework of RANS formulation, the $k$–$\omega$ SST [16], SA [17], and CLS [21] turbulence models are implemented to the flow solver. Of these models, the CLS model is originally an algebraic stress model with a cubic stress-strain relationship. However, it was observed that the success of the CLS model is dependent on the functional eddy viscosity coefficient of $C_\mu$ and not on the cubic stress-strain relationship [22,23]. Following this observation, the current study only adopts the formulation of the functional eddy viscosity. By leaving the stress-strain relationship linear, the flow solver can reduce the excessive computational cost entailed in the cubic model.

Dual time stepping is employed to obtain the second-order temporal accuracy as

$$\frac{\partial \hat{Q}}{\partial \tau} = -\hat{R}^{n+1,s+1} - \frac{3\hat{Q}^{n+1,s+1} - 4\hat{Q}^{n} + \hat{Q}^{n-1}}{2\Delta t} \tag{2}$$

where $\hat{R} = \frac{\partial(\hat{E}-\hat{E}_v)}{\partial \xi} + \frac{\partial(\hat{F}-\hat{F}_v)}{\partial \eta} + \frac{\partial(\hat{G}-\hat{G}_v)}{\partial \zeta}$. Here, $\tau$ represents pseudotime, $n$ is the physical time level, and $s$ is the pseudotime level. Equation (2) is then discretized in pseudotime using the Euler implicit method and is linearized using the flux Jacobian. This leads to the large system of linear equations in delta form at each pseudotime step as

$$\left(\frac{I}{J\Delta\tau} + \left[\frac{\partial \hat{R}}{\partial \hat{Q}}\right] + \frac{1.5I}{J\Delta t}\right)\Delta\hat{Q} = -\hat{R}^{n+1,s} - \frac{3\hat{Q}^{n+1,s} - 4\hat{Q}^{n} + \hat{Q}^{n-1}}{2J\Delta t} \tag{3}$$

The lower upper symmetric Gauss Seidel scheme [24] is used for the implicit time integration of Eq. (3). The viscous flux Jacobian in the implicit part is neglected because it does not influence the accuracy of computed solutions. Local time stepping is used during subiteration.

The modified advection upstream splitting method (AUSM) using pressure-based weight functions [25] is applied as a numerical flux at a cell interface. This scheme was designed to remove the nonmonotonic pressure oscillations of the AUSM-type schemes near a wall or behind shock waves by introducing pressure-based weighting functions at a cell interface. For higher-order spatial accuracy, the monotone upstream-centered schemes for conservation laws [26] approach is used. Primitive variables are extrapolated at a cell interface and the differentiable limiter [27] is employed to suppress unphysical oscillations near physical discontinuities.

### B. Dynamic Analysis

The definition of reference frames for dynamic analysis is depicted in Fig. 1. The $X$ axis denotes the axial direction and the $Z$ axis denotes the normal direction from the core rocket to the booster. Also, pitch angle is the rotation angle with respect to the $Y$ axis. The same notation is used throughout this paper.

The motion of the booster during separation can be described as follows. At first, the basic equations of rigid body motion with respect to the fixed coordinates of $XYZ$ are expressed as

$$\bar{F}_{cg} = \left(m\frac{\mathrm{d}\bar{v}}{\mathrm{d}t}\right)_{XYZ}, \qquad \bar{M}_{cg} = \left(\frac{\mathrm{d}\bar{h}}{\mathrm{d}t}\right)_{XYZ} \tag{4}$$

In Eq. (4), $\bar{F}_{cg}$ and $\bar{M}_{cg}$ are the external force and moment vectors because of aerodynamic force, gravity, and additional control force. $\bar{v}$ and $\bar{h}$ are velocity and angular momentum vectors with respect to the center of mass of the body.

Because the moment and product of inertia of the booster in the fixed coordinates would change continually due to its rotation, it is necessary to determine their values as functions of time. It is more convenient to use the body-fixed coordinates of $xyz$ for rotational description, whereas the force equations are directly solved in the fixed coordinates. Then the force and moment equations with an angular velocity $\bar{\omega}$ will finally result in the following forms of Euler's equations of motion:

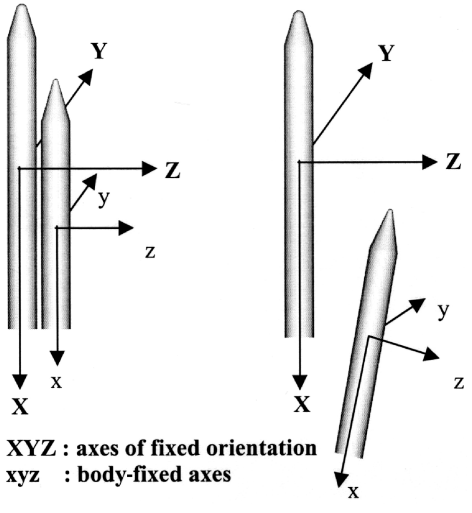


**Fig. 1 Reference frame.**

$$
\begin{aligned}
F_X &= m\dot{v}_X \qquad M_x = I_{xx}\dot{\omega}_x - (I_{yy} - I_{zz})\omega_y\omega_z \\
F_Y &= m\dot{v}_Y \qquad M_y = I_{yy}\dot{\omega}_y - (I_{zz} - I_{xx})\omega_z\omega_x \\
F_Z &= m\dot{v}_Z \qquad M_z = I_{zz}\dot{\omega}_z - (I_{xx} - I_{yy})\omega_x\omega_y
\end{aligned} \tag{5}
$$

From Eq. (5), the force equations yield the new velocity $\bar{v}^{n+1}$ and displacement $ds^{n+1}$ as

$$
\frac{\bar{v}^{n+1} - \bar{v}^n}{\Delta t} = \frac{1}{m}\bar{F}^n, \qquad ds^{n+1} = \tfrac{1}{2}(\bar{v}^n + \bar{v}^{n+1})\Delta t \tag{6}
$$

And the new angular momentum $\bar{\omega}^{n+1}$ and the angular displacement $d\alpha^{n+1}$ are updated as

$$
\begin{aligned}
\frac{\omega_x^{n+1} - \omega_x^n}{\Delta t} &= \frac{1}{I_{xx}}[M_x + (I_{yy} - I_{zz})\omega_y\omega_z] \\
\frac{\omega_y^{n+1} - \omega_y^n}{\Delta t} &= \frac{1}{I_{yy}}[M_y + (I_{zz} - I_{xx})\omega_z\omega_x] \\
\frac{\omega_z^{n+1} - \omega_z^n}{\Delta t} &= \frac{1}{I_{zz}}[M_z + (I_{xx} - I_{yy})\omega_x\omega_y] \\
d\alpha^{n+1} &= \frac{1}{2}(\bar{\omega}^n + \bar{\omega}^{n+1})\Delta t
\end{aligned} \tag{7}
$$

As a result, the new position and velocity component at the next time level are determined.

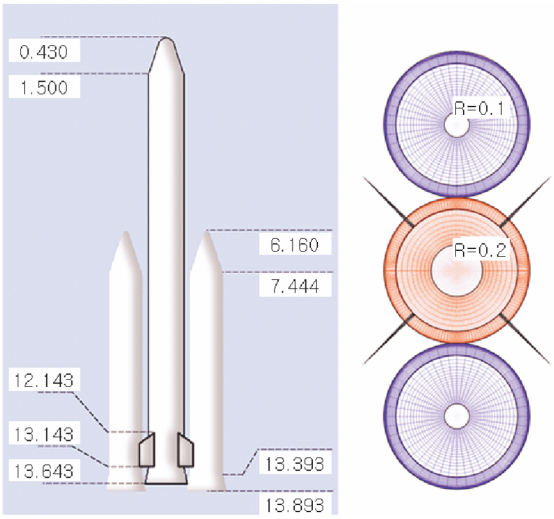


**Fig. 2 Configuration of the KSR-III.**

### C. Geometry Description and Mesh Generation

Figure 2 shows the geometry of the KSR-III launch vehicle. The KSR-III is composed of a core rocket and two strap-on boosters attached to the core. The strap-on boosters have the same diameter as the core rocket to employ the same rocket engine. The length of the strap-on boosters is about 57% of the core rocket. To prevent catastrophic contact between the core rocket and the boosters, the baseline of the booster is located 0.25 m lower than that of the core rocket. The fin of the core rocket has a thickness of 25 mm.

To represent the relative motion of bodies efficiently, the overset grid technique originally proposed by Steger et al. [28] is adopted. The trilinear interpolation technique with the Newton–Raphson method is used for donor cell searching. The main grids and subgrids of the overset grid system are generated as multiblock meshes to represent the fin and base regions. A detailed mesh system will be depicted in Sec. III.B.

## III. Results and Discussion

### A. Validation and Preliminary Studies

First, the steady-state flowfield of the Titan-IV launch vehicle is computed to validate the overset grid technique. Turbulent flow analysis is conducted using the $k$–$\omega$ SST model, and the freestream conditions are the Mach number of 1.6 and the Reynolds number of $1.1 \times 10^7$, with a zero angle of attack. The overlapping meshes of $101 \times 66 \times 121$ grid points for the core rocket and of $81 \times 66 \times 101$ for the booster are used. Figure 3 shows the cross-sectional pressure contour of the Titan-IV vehicle, and the computed surface pressure along the centerline of the vehicle is compared with the wind-tunnel data. A close agreement between experimental and computed values is observed except for a slight difference at the connecting point of the core rocket and the booster. In this region, the computed values are underestimated because of the effect of a connecting cable used in the wind-tunnel test [2].

Second, the separation motion of strap-on boosters in a simplified configuration is simulated to examine the influence of the base flow. The basic shape is similar to the KSR-III configuration, except that the model shape near the baseline is cylindrical without a fin and flare skirt. In this configuration, the dominant factor influencing the motion of the strap-on booster is the bow shock from the booster. A bow shock is first generated over the nose of the strap-on and then propagates to the core rocket. After hitting the surface of the core rocket, the shock impinges on the booster again. This mechanism sequentially increases the pressure on the left side of the strap-on, giving positive normal force and positive pitching moment. Here, it is assumed that a pressure change near the baseline is not critical, and thus the forebody analysis is expected to show a similar result to the full-body analysis.

Figures 4 and 5 show the results of the separation motion in the simplified configuration. Figure 4 is the computed pressure field. The initial distance between the core rocket and the booster is 0.2 m. Figure 5 shows the trajectory of the displacement and the rotation

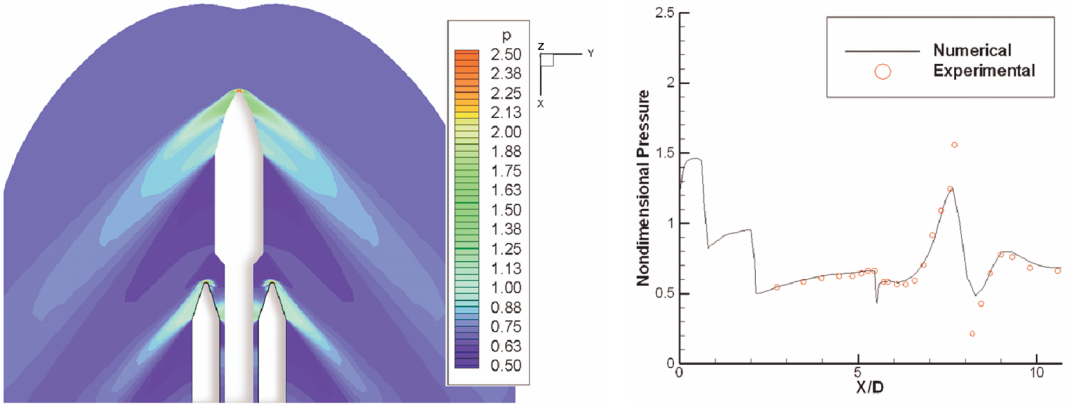


**Fig. 3 Pressure contour around the Titan-IV launch vehicle and surface pressure along the centerline (solid line: numerical result, circle: experimental data).**

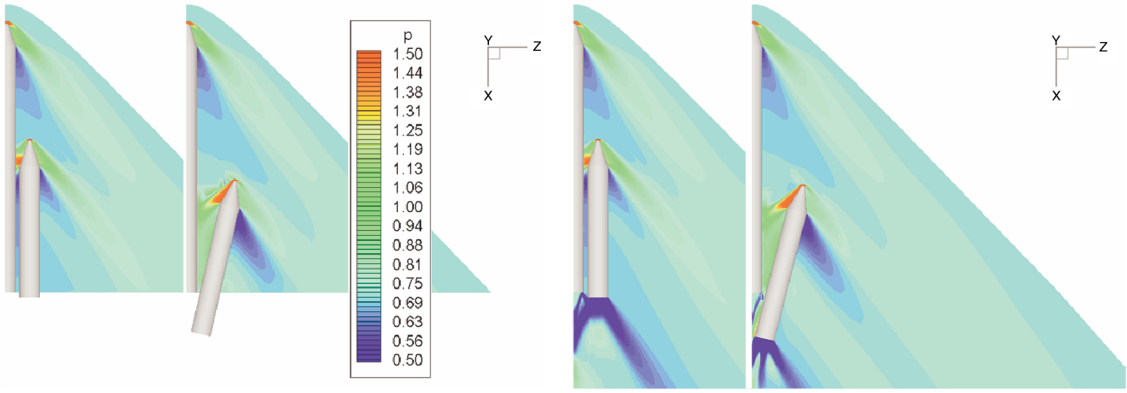


a) Forebody simulation b) Full-Body simulation

**Fig. 4 Separation motion of a simplified launch vehicle configuration (at t = 0.0 and 0.3 s).**

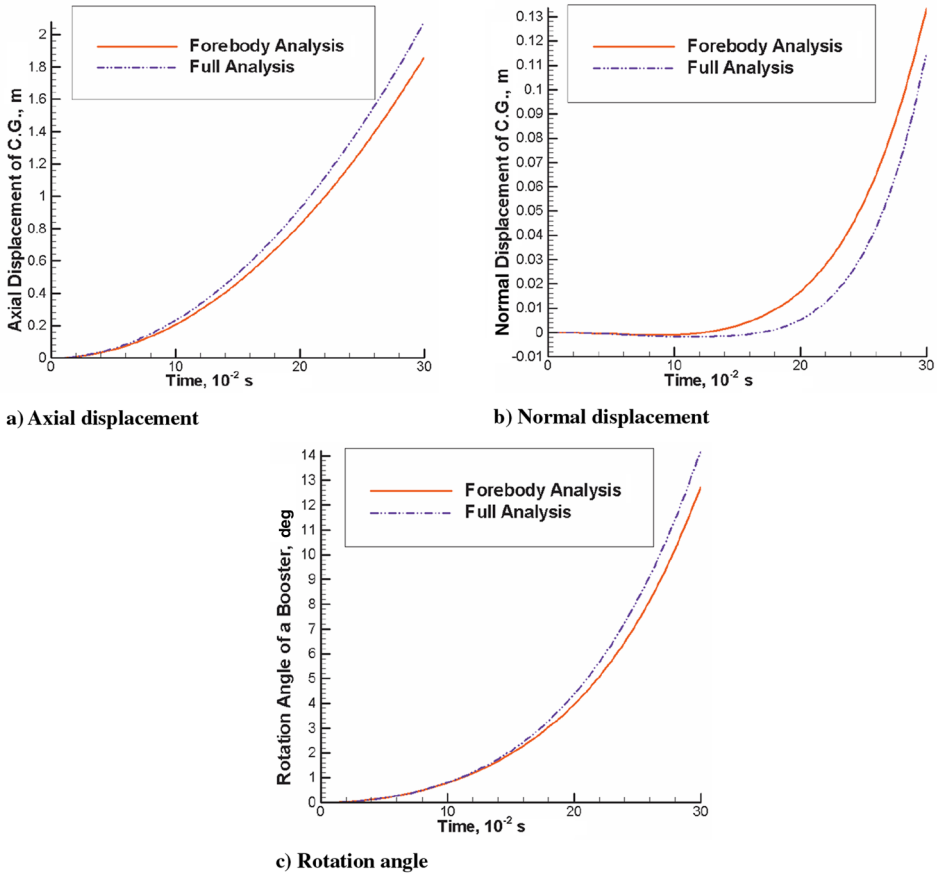


a) Axial displacement b) Normal displacement

c) Rotation angle

**Fig. 5 Position and rotation angle of the booster (solid line: forebody simulation, dashed line: full-body simulation).**

angle of the booster. As can be seen from the results, the full-body analysis yields a faster fall-down motion and rotation, as well as a slower repulsive motion. All of these characteristics can be explained by the role of expansion waves generated around the base region. Expansion waves lower the pressure at the base plane of the booster, which produces a faster fall-down speed than the forebody analysis. Also, expansion waves from the baseline of the core rocket reduce the pressure on the lower left side of the booster. As a result, the net normal force is relatively reduced, and the clockwise motion is accelerated because the part experiencing lower pressure is actually located below the center of mass of the booster. The effect of expansion waves from the core rocket and the booster can be observed clearly in Fig. 5. Even though the two analyses (forebody and full body) qualitatively exhibit the same tendency, they clearly yield different positions with time. Considering the base flow, downward motion and clockwise rotation are accelerated by about 10%, whereas normal displacement is decreased by about 15% at 0.3 s after separation.

Last, several turbulence models are applied to the analysis of a stand-alone booster of the KSR-III [29]. To accurately describe the massively separated flow in the base region, an advanced turbulence model is essential. At the same time, the enormous computational burden due to turbulence transport equations should be avoided. Thus, an accurate turbulence model with an acceptable computational cost is important for an efficient simulation of the separation motion of the rocket system. Here, inviscid and turbulent results are compared with the wind-tunnel test data compiled by the Korea Aerospace Research Institute to assess computational accuracy and efficiency. The analyses are performed at the Mach number of 1.6 and the Reynolds number of $1.683 \times 10^7$, with angles of attack of 0, 10, 20, and 30 deg. Based on the preliminary grid refinement tests, a two-block mesh with 1.5 million grid points is adopted as the

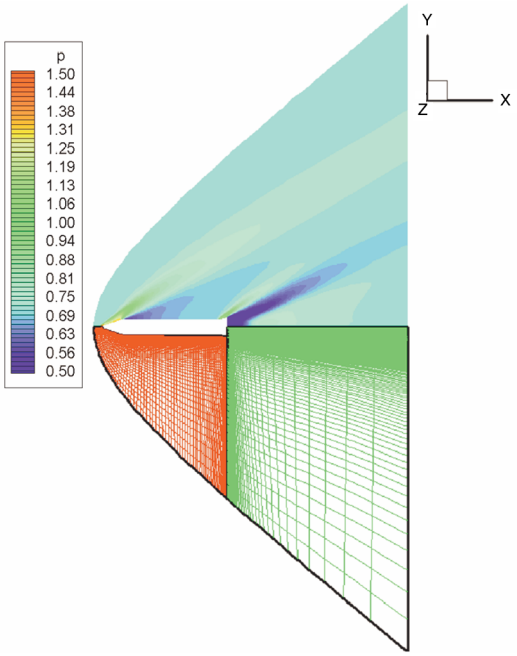


**Fig. 6 Mesh system and pressure contour around a stand-alone booster of the KSR-III.**

computation domain. The baseline of the rocket is assumed to be the solid wall. Figure 6 shows the mesh system and pressure contour at an angle of attack of 0 deg.

Tables 1–3 present computed aerodynamic coefficients at various angles of attack compared with the experimental data of Ok et al. [29]. Regarding the normal force and the pitching moment, all the simulations yield similar results, whereas some differences in the axial force can be observed between the inviscid and turbulent analyses. As expected, the turbulent simulations show better agreement with the experimental data.

Figure 7 shows the surface pressure distribution along the axial direction and the base pressure distribution along the radial direction at an angle of attack of 0 deg. In the case of the body surface distribution, all simulations show nearly the same results, except that the inviscid analysis predicts a slightly stronger oblique shock at the skirt. For the base pressure distribution, turbulent results are clearly more physical than the inviscid solution in the sense that the base flow usually does not exhibit a strong pressure gradient toward the radial direction at a 0 deg angle of attack. The mild pressure gradient in turbulent analyses is caused by the flow mixing inside the recirculation region due to turbulent kinetic energy. On the other hand, the inviscid computation shows a stronger pressure gradient in the base region and yields higher pressure at the stagnation point. Among the turbulence models, the CLS model predicts rather higher pressure than the $k$–$\omega$ SST model, as in Park et al. [23], and the SA model yields lower base pressure.

From the preliminary studies, the forebody-only simulation results in substantially different booster trajectories even in the simplified launch vehicle geometry. The effect of the afterbody region on the booster trajectory is expected to be more significant in the actual KSR-III shape. Also, the simulations of a stand-alone booster configuration show that turbulence mainly affects the axial force component, and the fall-down speed of the strap-on booster is expected to be faster in the turbulent analysis. Computed aerodynamic forces among the turbulence models are approximately the same. Thus, the $k$–$\omega$ SST model is adopted as the main turbulence model for unsteady motion simulation, because the $k$–$\omega$ SST model provides better convergence characteristics than other turbulence models.

### B. Separation Dynamics of the KSR-III

The steady-state aerodynamic characteristics of the KSR-III and the detachment motion of a strap-on during the separation process are examined. The freestream Mach number is 1.7 and the Reynolds number is $1.431 \times 10^7$. The flight angle with respect to the ground is 90 deg and the angle of attack is 0. During the separation, the core rocket constantly ejects plume gas through the nozzle exit, whereas the engine of the strap-on is extinguished just after separation. Thus,

**Table 1 Axial force coefficients of a stand-alone booster**

| Angle of attack | Trip-on experiment | Trip-off experiment | Inviscid | SA | CLS | $k$–$\omega$ SST |
|---|---|---|---|---|---|---|
| 0.0 | 0.64 | 0.62 | 0.579393 | 0.658066 | 0.638265 | 0.642174 |
| 10.0 | 0.69 | 0.66 | 0.638950 | 0.690538 | 0.667548 | 0.673245 |
| 20.0 | 0.72 | 0.70 | 0.684898 | 0.719355 | 0.713173 | 0.708900 |
| 30.0 | 0.76 | 0.74 | 0.733479 | 0.753686 | 0.758607 | 0.756455 |

**Table 2 Normal force coefficients of a stand-alone booster**

| Angle of attack | Trip-on experiment | Trip-off experiment | Inviscid | SA | CLS | $k$–$\omega$ SST |
|---|---|---|---|---|---|---|
| 0.0 | 0.0 | 0.0 | 0.0 | 0.0 | 0.0 | 0.0 |
| 10.0 | 0.72 | 0.64 | 0.780849 | 0.794824 | 0.814961 | 0.792976 |
| 20.0 | 2.58 | 2.57 | 2.499558 | 2.484706 | 2.490406 | 2.489458 |
| 30.0 | 4.67 | 4.61 | 4.574496 | 4.534726 | 4.541290 | 4.547741 |

**Table 3 Pitching moment coefficients of a stand-alone booster**

| Angle of attack | Trip-on experiment | Trip-off experiment | Inviscid | SA | CLS | $k$–$\omega$ SST |
|---|---|---|---|---|---|---|
| 0.0 | 0.0 | 0.0 | 0.0 | 0.0 | 0.0 | 0.0 |
| 10.0 | 1.66 | 1.75 | 1.725053 | 1.656376 | 1.647186 | 1.671261 |
| 20.0 | 3.00 | 2.94 | 2.944154 | 2.944198 | 2.939763 | 2.958803 |
| 30.0 | 4.10 | 4.04 | 3.973241 | 3.997101 | 3.997545 | 4.026465 |

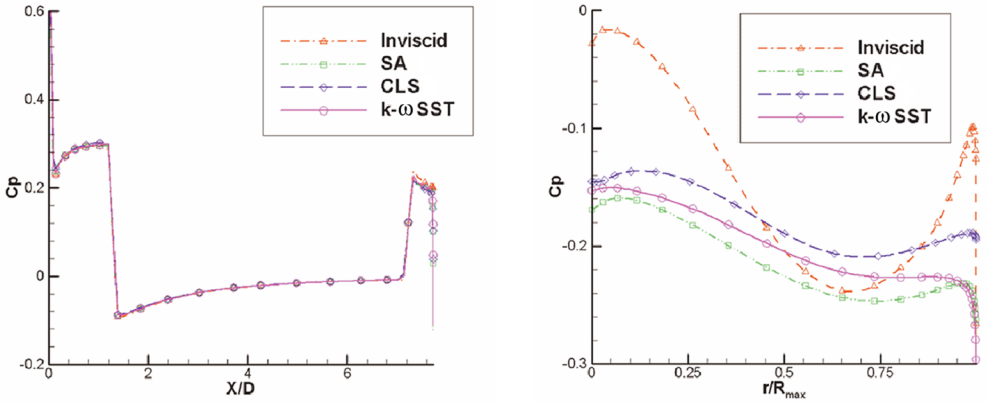


a) $C_p$ distribution along the body surface b) $C_p$ distribution on the base plane

**Fig. 7 Surface pressure on the forebody and base plane.**

the base plane of the booster is treated as a wall. As for the exit condition of the core rocket, flow properties at the nozzle exit are obtained by the chamber condition, which is described in the annual report of the KSR-III development. From the chamber condition and cold gas assumption, the properties at the exit are $Ma_{\text{exit}} = 2.86$ and $\frac{\rho}{\rho_{\text{inf}}} = \frac{p}{p_{\text{inf}}} = 1.084$. Other properties are calculated from these relations. Also, as the exit diameter of the nozzle is 746.4 mm, the center region of the base plane is treated as the nozzle exit and the outer region is assumed to be the wall. The boundary condition at the base plane is shown in Fig. 8.

As in Fig. 8, the main zones and subzones of the overlapping mesh system are constructed as multiblock meshes. The main grid for the core rocket has four blocks with about 2.8 million grid points. The computational region around the forebody of the core rocket is composed of three blocks to represent two fins with an X configuration. One more block is added for the base region of the core rocket. Similarly, the subgrid around the strap-on has two blocks with about 0.7 million grid points. One block mesh is generated around the forebody of the strap-on and another block is generated for the afterbody region of the booster. For efficient computation, parallel computing is conducted using 20 processors of a cluster machine with AMD 3800+ X2 CPUs.

In Fig. 9, pressure contours on and around the vehicle at the initial stage of separation are presented to investigate the aerodynamic characteristics of the launch vehicle and the initial motion of the booster. The first factor influencing the motion of the strap-on is the bow shock generated from the booster nose. The bow shock hits the core rocket and then turns back to the booster, which increases the pressure on the upper left side of the booster. As a result, the axial force and the repulsive force between the core rocket and the booster increase. In addition, a positive pitching moment is generated. The next factor influencing the motion of the strap-on is the oblique shocks from the core rocket. The oblique shocks generated at the fin and flare skirt of the core rocket hit the lower left side of the booster, resulting in a negative pitching moment and an increment in the normal force. Finally, expansion waves generated from the baseline of the core rocket also change the aerodynamic characteristics of the strap-on. Expansion waves hit the lower left side of the booster and somewhat counterbalance the effect of the oblique shock from the core rocket. All things combined, the strap-on initially experiences a repulsive force and a negative pitching moment. As a result, the strap-on moves away from the core rocket and rotates counterclockwise at the initial stage of the separation process, and a collision may occur depending on the magnitude of the negative pitching moment.

The separation motion of the strap-on booster is schematically summarized in Fig. 10. As mentioned, the booster initially experiences a negative pitching moment and starts a counterclockwise rotation. As the nose of the booster gets closer to the core rocket, the reflected bow shock becomes stronger and generates a strong repulsive force. At the same time, the oblique shock from the core rocket to the bottom of the booster gradually becomes weaker as the traveling distance of the oblique shock increases. Also, expansion waves from the baseline of the core rocket reduce the pressure at the strap-on. Thus, the booster is beginning to rotate in the opposite direction and it may avoid collision if the negative pitching moment at the initial stage is not too large. When the booster eventually gains a positive inclination angle, it tends to accelerate positive pitching motion mainly because the asymmetric bow shock of the nose produces a strong positive pitching moment. In addition, the negative pitching moment induced by the oblique shock from the core rocket is sufficiently diminished because the downward motion of the booster reduces the effective length of the moment arm with respect to the booster's center of gravity.

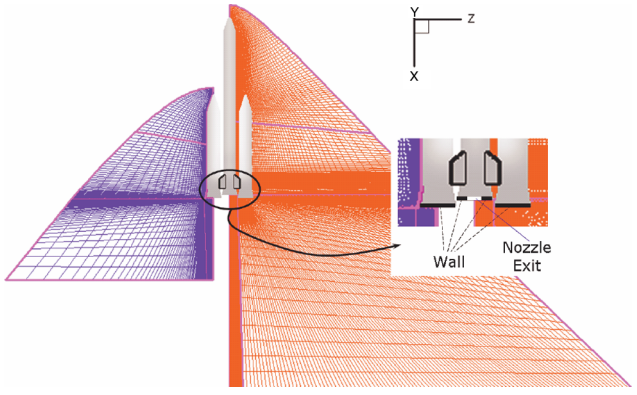


**Fig. 8 Overlapping mesh system and boundary condition at the base plane.**

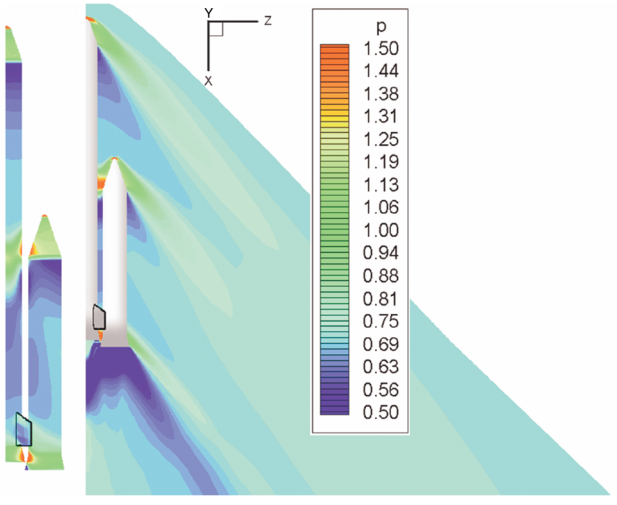


**Fig. 9 Pressure contour on and around the KSR-III.**

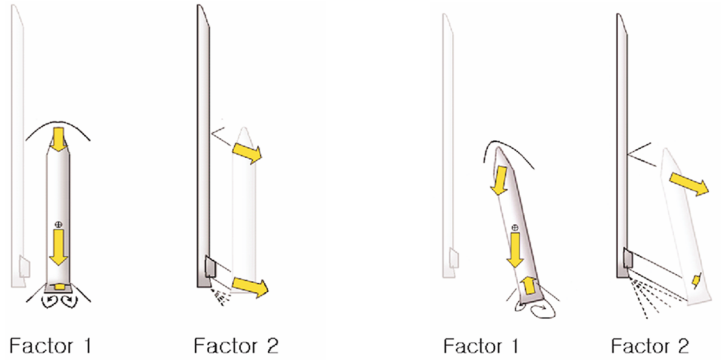


a) Initial stage

b) Intermediate stage

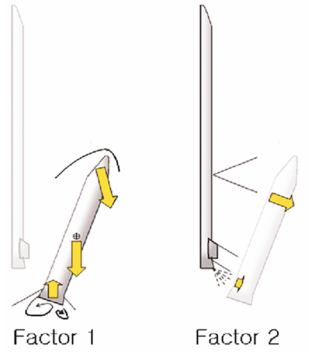


c) Final stage

**Principal Mechanisms**

- Factor 1: Forces Due to the Inclination of the Booster
  1) Bow Shock over the Nose
  2) Gravity
  3) Oblique Shock on the Skirt & Flow Separation in the Base
- Factor 2: Forces Due to Interaction with the Core Rocket
  1) Reflected Bow Shock
  2) Oblique Shocks from Fins and Skirts of the Core Rocket
  3) Expansion Waves from the Base of the Core Rocket

**Fig. 10 Schematics of the separation motion of the strap-on.**

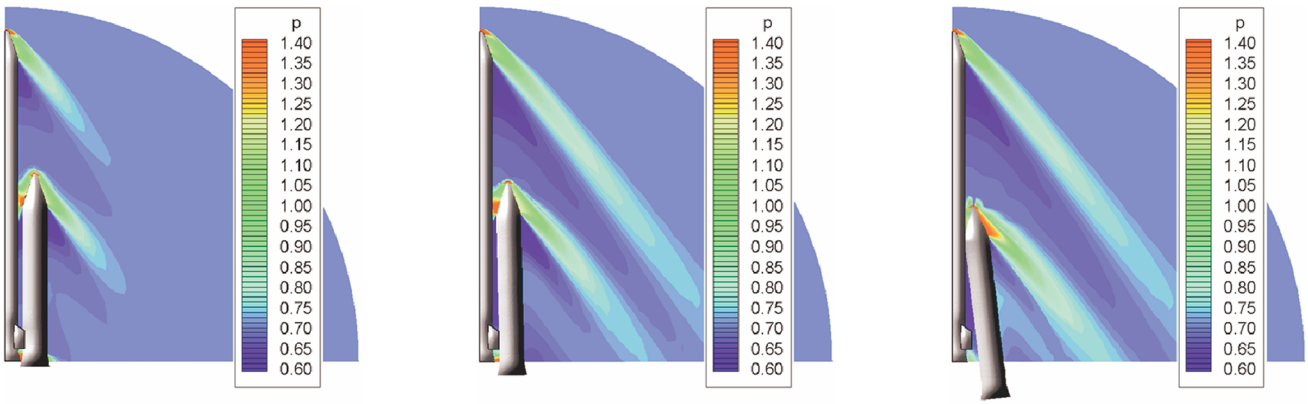


a) Initial pressure contour b) Pressure contour at 0.10 s c) Pressure contour at 0.20 s

**Fig. 11 Separation motion analysis in the forebody simulation (from 0.00 to 0.40 s, time interval of 0.20 s).**

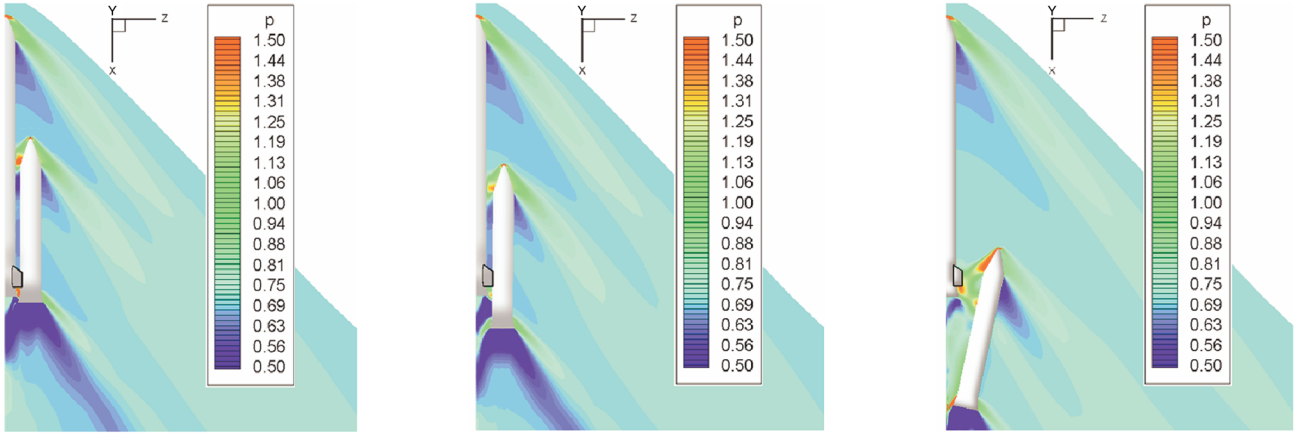


a) Initial pressure contour b) Pressure contour at 0.20 s c) Pressure contour at 0.40 s

**Fig. 12 Separation motion analysis including the base region (from 0.00 to 0.40 s, time interval of 0.20 s).**

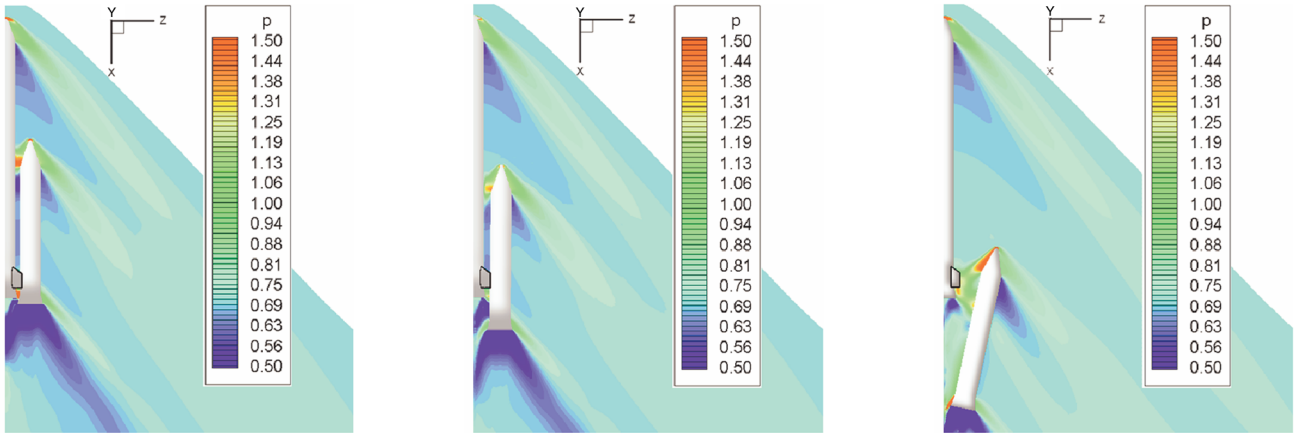


a) Initial pressure contour b) Pressure contour at 0.20 s c) Pressure contour at 0.40 s

**Fig. 13 Separation motion analysis using the $k$–$\omega$ SST model (from 0.00 to 0.40 s, time interval of 0.20 s).**

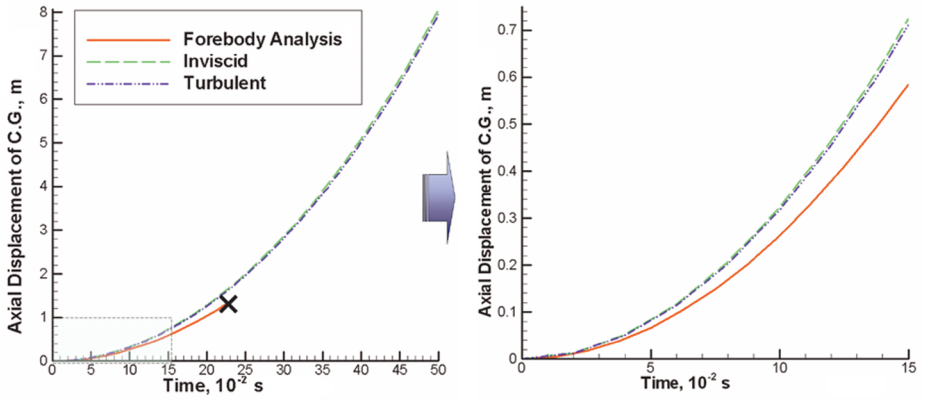


a) Axial displacement

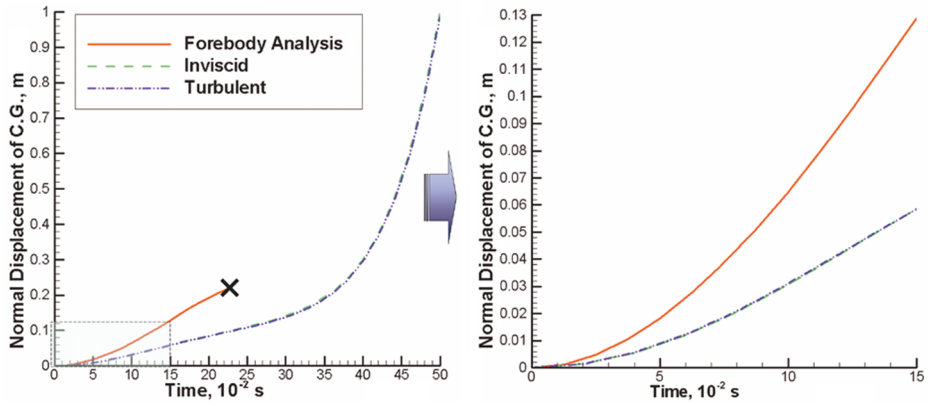


b) Normal displacement

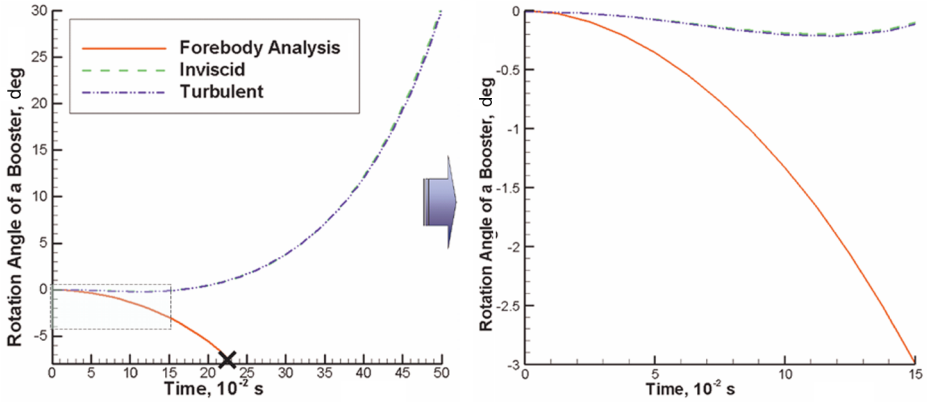


c) Rotation angle

**Fig. 14 Position and rotation angle of the booster during separation (solid line: forebody simulation, dashed line: inviscid, dash dot dot: turbulent).**

The separation dynamics of the KSR-III are examined. Analyses are performed using the dual time stepping method, with the physical time step of 0.005 s. Also, all simulations exhibit the free-fall motion of a booster, that is, no jettisoning force on the booster. The base effect on the trajectory of the booster is investigated first. The pressure fields of the forebody and full-body inviscid simulations are compared in Figs. 11 and 12. From the results, the full-body analysis shows a faster fall-down motion than the forebody simulation and exhibits a positive pitching moment. As explained previously, this is a consequence of the interactions between the bow shock from the booster nose, the oblique shocks from the fin and skirt of the core rocket, the expansion waves from the core rocket, and the base pressure. In the case of the forebody simulation, the base region moves completely out of the computational domain as separation proceeds. This means that high surface pressure induced by the oblique shocks will remain unchanged and the booster will produce an excessive negative pitching moment. As a result, the forebody simulation shows the collision between the core rocket and the strap-on booster at 0.22 s after the separation, whereas the full-body simulation yields no collision. As shown in Fig. 12, the booster initially starting with the counterclockwise rotation reverses its rotating direction during separation and is finally postured with a positive angle of attack. Then, the body accelerates the clockwise rotation and finally leads to a safe separation.

Next, the detachment motion of the strap-on booster in the turbulent flowfield is examined. Figure 13 shows the trajectory and pressure field at free separation. As can be seen in Figs. 12 and 13, both inviscid and turbulent analyses provide very similar pressure fields and no visible difference between the two solutions can be found. This is because, in the separation dynamics of strap-on boosters, the effect of nonlinear waves is much stronger than the viscous effect, and the second-order numerical dissipation in the convective flux somewhat mimics the physical viscosity. Figure 14 shows the temporal trajectories of the position and rotation angle. Inviscid and turbulent results exhibit nearly the same behavior, whereas the forebody analysis drastically deviates. During the separation process, the difference in position and rotation angle between the two simulations always stays within 2.5%.

As in Fig. 14b, a slightly slower downward motion of the booster in the turbulent analysis may appear contradictory to the previous result of the stand-alone booster analysis, in which turbulent analysis provided larger axial force. As can be seen in Fig. 15, the high-pressure region around the skirt of the booster is more diffused in the turbulent result than the inviscid case. As a result, the inviscid analysis slightly overestimates the high pressure around the skirt, and a higher axial force is obtained.

## IV. Conclusions

Aerodynamic dynamic coupled analysis is carried out for the accurate simulation of separation dynamics of strap-on boosters in a launch vehicle configuration. In particular, the influence of the base region and the effect of turbulence on the dynamic behavior of the booster are examined. From the preliminary study, flow analysis ignoring the afterbody region can result in a false scenario even with a simple launch vehicle configuration. Among the tested turbulence models, the $k$–$\omega$ SST model is proven to be the most appropriate to adequately and efficiently describe the RANS-based turbulent flowfields around a launch vehicle configuration.

Based on the preliminary study, the booster separation of the KSR-III is examined. At the initial stage, the booster experiences a negative pitching moment but gradually recovers a positive pitching moment, and this finally leads to a safe separation. Unlike the full-body analysis, the forebody analysis does not capture the interactions between the bow shock from the nose, the oblique shocks from the fin and flare skirt, the expansion waves on the baseline, and the base

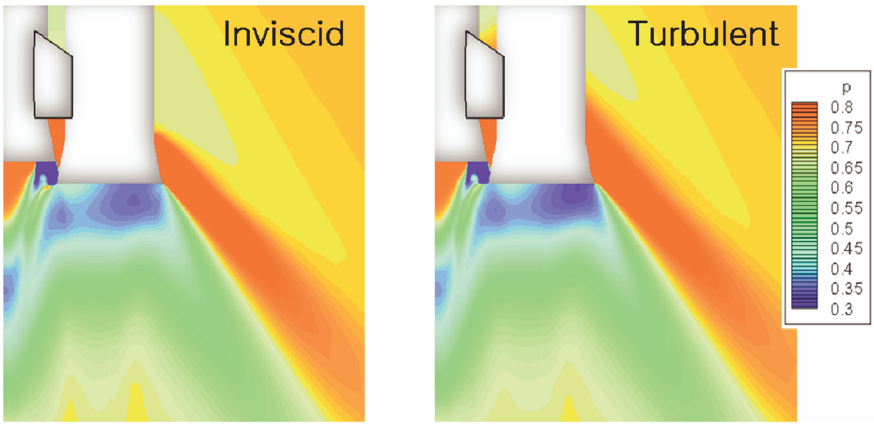


**a) At t = 0.0 s**

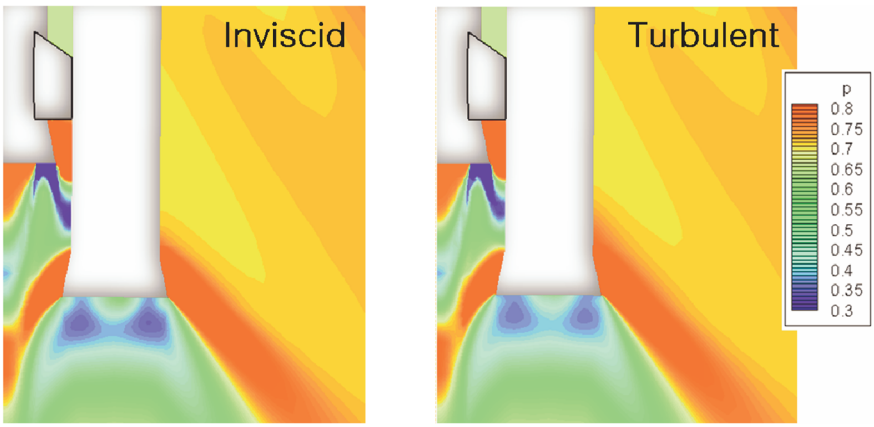


**b) At t = 0.2 s**

**Fig. 15 Comparison of computed flowfields between inviscid and turbulent analyses.**

pressure. As a result, it leads to a false collision scenario between the core rocket and the booster.

As for the viscous effect, the turbulent analysis shows nearly the same result as the inviscid analysis. In the inviscid analyses, both the movement and rotation of the booster deviate only slightly from the turbulent cases. Thus, inviscid analysis seems to be sufficient for the efficient simulation of the separation motion of strap-ons. Finally, the present work demonstrates that the prototype KSR-III configuration yields a safe separation even in a free-fall condition, but an additional jettisoning force would be necessary for unpredicted external disturbance during separation.

## Acknowledgments

The authors would like to acknowledge the computing support of the Korea Institute of Science and Technology Information (KISTI) under "The Sixth Strategic Supercomputing Support Program," with Kum Won Cho as the technical supporter. Also, the authors would like to acknowledge the financial support of the Bain Korea-21 program for the School of Mechanical and Aerospace Engineering Research at Seoul National University and the Korea National e-Science project.

## References

[1] Palmer, G., Buning, P., Yanowitz, H., and Venkatapathy, E., "Three-Dimensional Computational Analysis of Complex Launch Vehicle Configurations," *Journal of Spacecraft and Rockets*, Vol. 33, No. 1, 1996, pp. 49–53.

[2] Taylor, S., and Wang, J. C. T., "Launch-Vehicle Simulations Using a Concurrent, Implicit Navier–Stokes Solver," *Journal of Spacecraft and Rockets*, Vol. 33, No. 5, 1996, pp. 601–606.

[3] Azevedo, J. L. E., Moraes, P., Jr., Maliska, C. R., Marchi, C. H., and Silva, A. E. C., "Code Validation for High-Speed Flow Simulation over Satellite Launch Vehicle," *Journal of Spacecraft and Rockets*, Vol. 33, No. 1, 1996, pp. 15–21.

[4] Meakin, R. L., and Suhs, N. E., "Unsteady Aerodynamic Simulation of Multiple Bodies in Relative Motion," AIAA Paper 89-1996, 1989.

[5] Lochan, R., Adimurthy, V., and Kumar, K., "Separation Dynamics of Strap-On Boosters in the Atmosphere," *Journal of Guidance, Control, and Dynamics*, Vol. 20, No. 4, 1997, pp. 633–639.

[6] Gea, L. M., and Vicker, D., "CFD Simulations of the Space Shuttle Launch Vehicle with Booster Separation Motor and Reaction Control System Plumes," *Computational Fluid Dynamics 2004: Proceedings of the Third International Conference on Computational Fluid Dynamics*, Springer Verlag, Berlin/New York/Heidelberg, 2006, pp. 233–238.

[7] Chan, W., Meakin, R., and Potsdam, M., "CHSSI Software for Geometrically Complex Unsteady Aerodynamic Applications," AIAA Paper 2001-0539, 2001.

[8] Lijewski, L. E., and Suhs, N. E., "Time-Accurate Computational Fluid Dynamics Approach to Transonic Store Separation Trajectory Prediction," *Journal of Aircraft*, Vol. 31, No. 4, 1994, pp. 886–891.

[9] Murman, S. M., Aftosmis, M. J., and Berger, M. J., "Simulation of 6-DOF Motion with a Cartesian Method," AIAA Paper 2003-1246, 2003.

[10] Choi, S. J., Kim, C., Rho, O. H., and Park, J. J., "Numerical Analysis on Separation Dynamics of Strap-On Boosters in the Atmosphere," *Journal of Spacecraft and Rockets*, Vol. 39, No. 3, 2002, pp. 439–446.

[11] Meakin, R. L., "A General Simulation Method for Multiple Bodies in Proximate Flight," AIAA Paper 2003-3831, 2003.

[12] Bigarella, E. D., and Azevedo, J. L., "Numerical Study of Turbulent Flows over Launch Vehicle Configurations," *Journal of Spacecraft and Rockets*, Vol. 42, No. 2, 2005, pp. 266–276.

[13] Liu, X., and Fu, S., "Numerical Simulation of Compressible Separated Turbulent Flows over Inclined Slender Body," *Journal of Spacecraft and Rockets*, Vol. 42, No. 3, 2005, pp. 572–575.

[14] Bigarella, E. D., Azevedo, J. L., and Scalabrin, L. C., "Centered and Upwind Multigrid Turbulent Flow Simulations of Launch Vehicle Configurations," *Journal of Spacecraft and Rockets*, Vol. 44, No. 1, 2007, pp. 52–65. doi:10.2514/1.23843

[15] Pamadi, B., Neirynck, T., Hotchko, N., Scallion, W., Murphy, K., and Covell, P., "Simulation and Analyses of Stage Separation of Two-Stage Reusable Launch Vehicles," *Journal of Spacecraft and Rockets*, Vol. 44, No. 1, 2007, pp. 66–80. doi:10.2514/1.17896

[16] Menter, F. R., "Two-Equation Eddy-Viscosity Turbulence Models for Engineering Applications," *AIAA Journal*, Vol. 32, No. 8, 1994, pp. 1598–1605.

[17] Spalart, P. R., and Allmaras, S. R., "A One-Equation Turbulence Model for Aerodynamic Flows," AIAA Paper 92-0439, 1992.

[18] Kim, S., Kim, C., Rho, O. H., and Hong, S. K., "Cures for the Shock Instability: Development of a Shock-Stable Roe Scheme," *Journal of Computational Physics*, Vol. 185, No. 2, 2003, pp. 342–374. doi:10.1016/S0021-9991(02)00037-2

[19] Lee, B. J., and Kim, C., "Automated Design Methodology of Turbulent Internal Flow Using Discrete Adjoint Formulation," *Aerospace Science and Technology*, Vol. 11, Nos. 2 3, 2007, pp. 163–173. doi:10.1016/j.ast.2006.12.001

[20] Lee, J. I., Kim, C., and Kim, K. H., "Accurate Computations of Arc-Heater Flows Using Two-Equation Turbulence Models," *Journal of Thermophysics and Heat Transfer*, Vol. 21, No. 1, 2007, pp. 67–76. doi:10.2514/1.25495

[21] Craft, T. J., Launder, B. E., and Suga, K., "Development and Application of a Cubic Eddy-Viscosity Model of Turbulence," *International Journal of Heat and Fluid Flow*, Vol. 17, No. 2, 1996, pp. 108–115. doi:10.1016/0142-727X(95)00079-6

[22] Barakos, G., and Drikakis, D., "Numerical Simulation of Transonic Buffet Flows Using Various Turbulence Closures," *International Journal of Heat and Fluid Flow*, Vol. 21, No. 5, 2000, pp. 620–626. doi:10.1016/S0142-727X(00)00053-9

[23] Park, S. H., Acharya, S., and Kwon, J. H., "An Improved Formulation of $k$–$\varepsilon$ Turbulence Models for Supersonic Base Flow," AIAA Paper 2005-4707, 2005.

[24] Yoon, S., and Jameson, A., "Lower-Upper Symmetric Gauss–Seidel Method for the Euler and Navier–Stokes Equations," *AIAA Journal*, Vol. 26, No. 9, 1988, pp. 1025–1026.

[25] Kim, K. H., Kim, C., and Rho, O. H., "Methods for the Accurate Computations of Hypersonic Flows, Part 1: AUSMPW+ Scheme," *Journal of Computational Physics*, Vol. 174, No. 1, 2001, pp. 38–80. doi:10.1006/jcph.2001.6873

[26] Van Leer, B., "Towards the Ultimate Conservative Difference Scheme. 5. A Second-Order Sequel to Godunov's Methods," *Journal of Computational Physics*, Vol. 32, No. 1, 1979, pp. 101–136. doi:10.1016/0021-9991(79)90145-1

[27] Anderson, W. K., Thomas, J. L., and Van Leer, B., "Comparison of Finite Volume Flux Vector Splittings for the Euler Equations," *AIAA Journal*, Vol. 24, No. 9, 1986, pp. 1453–1460.

[28] Steger, J. L., Dougherty, F. C., and Benek, J. A., "A Chimera Grid Scheme," *Advances in Grid Generation*, FED Vol. 5. American Society of Mechanical Engineers, Fairfield, NJ, 1983, pp. 59–69.

[29] Ok, H., Kim, I., Ra, S. H., Choi, S. W., Oh, B. S., and Lee, J., "Determination of the Separation Forces of the Strap-On Boosters," AIAA Paper 2004-874, 2004.

R. Cummings
*Associate Editor*